

**Understanding Formation Thermodynamics of Structurally Diverse Zeolite Oligomers with First Principles Calculations**

Journal:	<i>Dalton Transactions</i>
Manuscript ID	DT-ART-08-2022-002764.R1
Article Type:	Paper
Date Submitted by the Author:	21-Dec-2022
Complete List of Authors:	Hong, Sungil; University of Pittsburgh, Chemical Engineering Malette, Adam; University of Houston, Chemical and Biomolecular Engineering Neeway, James; Pacific Northwest National Laboratory, Geosciences Motkuri, Radha; Pacific Northwest National Laboratory (PNNL), Applied Functional Materials Rimer, Jeffrey; University of Houston, Chemical and Biomolecular Engineering Mpourmpakis, Giannis; University of Pittsburgh, Chemical and Petroleum Engineering

# Understanding Formation Thermodynamics of Structurally Diverse Zeolite Oligomers with First Principles Calculations

Sungil Hong<sup>1</sup>, Adam J. Mallette<sup>2</sup>, James J. Neeway<sup>3</sup>, Radha Kishan Motkuri<sup>3</sup>, Jeffrey D. Rimer<sup>2</sup>,  
and Giannis Mpourmpakis<sup>1,\*</sup>

<sup>1</sup>Department of Chemical and Petroleum Engineering, University of Pittsburgh, Pittsburgh, PA, 15261, USA.

<sup>2</sup>Department of Chemical and Biomolecular Engineering, University of Houston, Houston, TX, 77204, USA

<sup>3</sup>Energy and Environment Directorate, Pacific Northwest National Laboratory, Richland, WA, 99352, USA

Corresponding author's e-mail: gmpourmp@pitt.edu

## Abstract

The mechanisms of many zeolitic processes, including nucleation and interzeolite transformation are not fully understood owing to complex growth mixtures that obfuscate in situ monitoring of molecular events. In this work, we provide insights into zeolite chemistry by investigating the formation thermodynamics of small zeolitic species using first principles calculations. We systematically study how formation energies of pure-silicate and aluminosilicate species differ by structure type and size, temperature, and the presence of alkali or alkaline earth metal cations ( $\text{Na}^+$ ,  $\text{K}^+$ , and  $\text{Ca}^{2+}$ ). Highly condensed (cage-like) species are found to be strongly preferred to simple rings in the pure-silicate system, and this thermodynamic preference increases with temperature. Introducing aluminum leads to more favorable formation thermodynamics for all species. Moreover, with a low Si/Al ratio ( $\leq 2$ ), a thermodynamic preference no longer exists among structure types and a pool of diverse aluminosilicate structures compete in formation. Metal cation effects strongly depend on the presence of aluminum, cage size, cation type, and location since each of these factors can alter electrostatic interactions between cation and zeolitic species. We reveal that confined metal cations may destabilize pure-silicate cages due to localized interactions; conversely, they stabilize aluminosilicates due to strong cation-framework attractions in sufficiently large cages. Importantly, this work rationalizes a series of experimental observations and can potentially guide efforts for controlling zeolite nucleation/crystallization processes.

## 1. Introduction

Elucidating mechanisms of nucleation and growth of zeolites, including interzeolite transformations, remain one of the most difficult challenges for controlling zeolite synthesis outcomes. An early concept introduced by Barrer and coworkers postulated that zeolite crystals could directly result from the sequential addition of prefabricated building units, which was based on the observation that the crystals are composed of small repeating units<sup>1</sup>. Through technological advances in spectroscopy (Raman, Infrared, and NMR) over several decades, it became possible to identify silicate speciation in solution<sup>2-6</sup>. Notably, some research groups observed strong structural similarities between the soluble species and final crystals, which directly supported the idea of the “assembly of precursors”<sup>7-11</sup>. However, both the mechanism and the supporting evidence have been disputed in literature<sup>12-15</sup>. For instance, Houssin et al.<sup>11</sup> proposed new molecular precursors (pentacyclic dodecamer) for MFI-type zeolites based on <sup>29</sup>Si NMR spectra, but Knight et al.<sup>15</sup> pointed out that the peaks ascribed to such precursors arise from smaller soluble species, and therefore the existence of the precursors was not fully supported. In fact, none of the ~40 unique silicate structures that have been confirmed are composed of more than 9 silicon atoms, and no “molecular precursor” exists exclusively for a targeted topology<sup>12, 14-16</sup>. This shows that there is no clear correlation between the soluble species and resulting zeolite crystals, which appears to contradict the assembly mechanism. Instead, potential alternative mechanisms for zeolite crystallization have been suggested including: (1) the release of small soluble species from an amorphous gel into the solution phase and their nucleation to grow crystals<sup>17, 18</sup>, and (2) the reorganization of amorphous structures towards crystals via breakage and recombination of siloxane bonds under hydrothermal conditions<sup>19-21</sup>. The crystallization of zeolites involves kinetic processes that are highly affected by many factors (e.g., temperature, cation, elemental composition, and source selection for silicon and aluminum). Therefore, revealing zeolite formation mechanisms requires integrated observations and knowledge in a wide range of zeolitic structures in multiple phases, from aqueous oligomers to solid particles.

Examining amorphous/crystalline solid particles that appear during a crystallization process is no longer technically limited owing to the advances in microscopy and crystallography<sup>22, 23</sup>. In contrast, small solution species are difficult to study experimentally. Although there have been extensive efforts to identify (alumino)silicate species in solution using spectroscopies<sup>3-6, 24-27</sup>, our understanding of the molecular events during zeolite nucleation processes is limited due to the

hurdles of in situ monitoring. Thus, theoretical studies have been carried out using quantum mechanical methods<sup>28-31</sup> and kinetic simulations<sup>32-34</sup>. Especially, the initial stage of nucleation, i.e., oligomerization of silicate monomers ( $\text{Si}(\text{OH})_4$ ) and cyclization of linear oligomers, has been of particular interest. Most of the studies<sup>29-34</sup> have focused on the formation of up to tetrameric species (consisting of 4 tetrahedral (T) atoms), since they are abundant in solution and do not require high computational cost to simulate. However, mid-sized species (i.e., larger than 4 T-units but smaller than experimentally accessible solid particles) have not attracted much attention, albeit they are also essential for understanding zeolite chemistry. Therefore, theoretical investigation of species falling into the mesoscale range is necessary to fill the gap in our understanding of how zeolite precursors evolve.

Furthermore, the building units that appear in topologies but not in solution (many composite building units (CBUs) and secondary building units (SBUs); for example, double-6-membered ring (*d6r*) or hexagonal prism) contain information of a particular framework since its geometry and topology result from thermodynamics and kinetics of nucleation/growth processes. For instance, Blatov and coworkers proposed a packing model of zeolite building units, which explained why only a limited number of zeolites have been experimentally realized out of millions of hypothetical zeolites<sup>35</sup> and predicted the existence of zeolites that have not been synthesized yet<sup>36</sup>. Moreover, zeolite building units are putatively of great importance in interzeolite transformation. There are many transformation pairs that share a CBU (e.g., *d6r* in LEV-to-CHA conversion<sup>37</sup> and *mor* for BEA-to-MFI<sup>38</sup>). It was found that there is a remarkable similarity in graph representation of the transformation pairs that do have a common CBU<sup>39</sup>, which indicates that geometry may play a significant role in transformation processes.

Understanding the role of cations during zeolite crystallization and interzeolite transformation processes is also of high importance. Zeolites are always produced in the presence of cations, which can significantly affect crystallization chemistry<sup>40</sup> and physicochemical properties of the products<sup>41</sup>. The roles of extra-framework cations include counterbalancing negative framework charges that result from the presence of trivalent atoms in tetrahedrally coordinated environments (e.g.,  $\text{Al}^{3+}$  and  $\text{Fe}^{3+}$ )<sup>20</sup>, and directing the formation of target topologies<sup>42</sup>. While alkali metal cations ( $\text{Na}^+$ ,  $\text{K}^+$ ,  $\text{Cs}^+$ , etc.) are the most common in naturally occurring or synthetic zeolites, highly siliceous zeolite crystals ( $\text{Si}/\text{Al} > 10$ ) typically require cationic organic structure-directing agents (OSDAs)<sup>42-45</sup>. Since siliceous zeolites have low framework charge and intrinsic hydrophobicity,

bulky organic cations can direct these frameworks effectively by simultaneously filling pores and compensating for negative framework charges<sup>46-49</sup>. Despite their effectiveness, OSDAs suffer from high synthesis costs and significant pollution during their removal<sup>50</sup>, which has spurred extensive efforts towards OSDA-free synthesis, often by introducing seed crystals to direct desired products<sup>46, 49, 51-54</sup>. Although the mechanism of the process has not been fully understood, it has been suggested that the transformation is mediated by zeolitic species in a solution phase. Kamimura and coworkers claimed that the dissolved fragments of zeolite beta (\*BEA) seeds in alkaline solution induce zeolite MTW crystallization<sup>54</sup>. Similarly, Zhang et al. showed small building units originating from zeolite CDO seed crystals enable OSDA-free synthesis of FER-type zeolites<sup>51</sup>, where the interactions between the fragments and alkali metal cations play a key role<sup>55</sup>. Furthermore, Tendeloo et al. reported that FAU crystals could evolve to four different topologies (ABW, CHA, MER, and ANA) depending on which alkali species is present ( $\text{Li}^+$ ,  $\text{K}^+$ ,  $\text{Rb}^+$ , and  $\text{Cs}^+$ , respectively)<sup>56</sup>. These findings demonstrate that a better understanding of the interactions between zeolitic species and inorganic cations is crucial for effectively controlled zeolite syntheses.

Herein, we use first principles calculations to understand the formation thermodynamics of structurally diverse zeolitic oligomers that are relevant to a wide range of zeolite synthesis and transformation processes. First, we explore how the formation energy of zeolitic species depends on the structure type (from simple rings to cages), structure size, temperature, and the presence of framework aluminum. Next, we investigate the effects of select alkali and alkaline earth metal cations on the formation thermodynamics of cage structures. The formation energy profiles provided herein reveal a thermodynamic preference for growth of (alumino)silicates under hydrothermal conditions. Also, our calculations rationalize the wider window of experimentally accessible Al-rich zeolite crystals compared to that of highly siliceous crystals<sup>57</sup>. Moreover, we unravel effects from inorganic cations in the formation thermodynamics of pure-silicate/aluminosilicate cages, shedding light on the roles and limitations of cations for directing target zeolite frameworks. Taken together, our results rationalize the presence of zeolitic species and frameworks under specific experimental conditions and compositions, which can guide experimental efforts to efficiently synthesize a wide range of zeolite crystals.

## 2. Computational Details

Density functional theory (DFT) calculations were performed using the Gaussian 09 software package<sup>58</sup>. The M062X functional coupled with split-valance triple-zeta basis set with polarizable functions 6-311G(d,p) was used since it has been shown to accurately describe main-group chemistry<sup>59</sup>. In order to address a typical hydrothermal environment of zeolite synthesis, calculations were carried out applying implicit solvation model, the conductor-like polarizable continuum model or CPCM<sup>60</sup>, having water as a solvent. Thermochemistry was applied at three different temperatures (50, 100, and 150 °C; specified in results) as implemented in Gaussian 09<sup>61</sup> to address thermal effects. Frequency calculations were performed after full optimization to calculate Gibbs free energy and verify that the structures were minima of the potential energy surfaces by the absence of any imaginary frequencies. Pure-silicate/aluminosilicate structures are assumed to form via condensation reactions of silicate monomers (or silicic acid, Si(OH)<sub>4</sub>) and aluminate monomers (Al(OH)<sub>3</sub>(H<sub>2</sub>O)), which release one water molecule per condensation reaction. Therefore, all silicate and aluminate species are terminated with hydroxyls and aluminum has one terminal water (to retain the tetrahedral coordination and due to the high affinity of Al for water molecule). We also considered the presence of a cation (Na<sup>+</sup>, K<sup>+</sup>, or Ca<sup>2+</sup>), which is assumed to incorporate via condensation between a (alumino)silicate structure and cation hydroxide (NaOH, KOH, or Ca(OH)<sub>2</sub>), resulting in charge-neutral species. More specifically, hydroxyl(s) from the cation hydroxide react(s) with the hydrogen atom(s) on the terminal hydroxyl (on Si) or water (on Al) on the zeolitic clusters to generate water. The Gibbs free energy of formation ( $\Delta G_f$ ) is determined by equations (1-4), depending on the structure type formed (monocycles, multicycles, and cages; see Table 1 for the description of each structure type):

$$\Delta G_{f,\text{monocycle}} = \frac{G_{\text{Si}_x\text{Al}_y\text{O}_{3(x+y)}\text{H}_{2x+3y}} + (x+y)G_{\text{H}_2\text{O}} - xG_{\text{Si(OH)}_4} - yG_{\text{Al(OH)}_3(\text{H}_2\text{O})}}{x+y} \quad (1)$$

$$\Delta G_{f,\text{multicycle (complete)}} = \frac{G_{\text{Si}_x\text{Al}_y\text{O}_{\frac{5(x+y)}{2}+2}\text{H}_{x+2y+4}} + \left(\frac{3(x+y)}{2} - 2\right)G_{\text{H}_2\text{O}} - xG_{\text{Si(OH)}_4} - yG_{\text{Al(OH)}_3(\text{H}_2\text{O})}}{x+y} \quad (2)$$

$$\Delta G_{f,\text{multicycle (branched)}} = \frac{G_{\text{Si}_x\text{Al}_y\text{O}_{\frac{5(x+y)}{2}+\frac{5}{2}}\text{H}_{x+2y+5}} + \left(\frac{3(x+y)}{2} - \frac{5}{2}\right)G_{\text{H}_2\text{O}} - xG_{\text{Si(OH)}_4} - yG_{\text{Al(OH)}_3(\text{H}_2\text{O})}}{x+y} \quad (3)$$




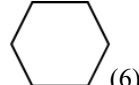

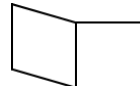
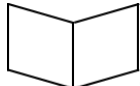

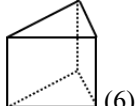
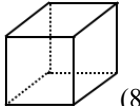
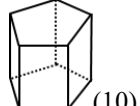
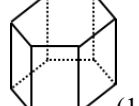
$$\Delta G_{f,\text{cage}} = \frac{G_{\text{Si}_x\text{Al}_y\text{O}_{\frac{5(x+y)}{2}}\text{H}_{x+2y-iz}\text{M}_i} + \left(\frac{3(x+y)}{2} + iz\right)G_{\text{H}_2\text{O}} - xG_{\text{Si(OH)}_4} - yG_{\text{Al(OH)}_3(\text{H}_2\text{O})} - iG_{\text{M(OH)}_z}}{x+y} \quad (4)$$

where  $G$  stands for the Gibbs free energy of a species, and  $x$  and  $y$  are the numbers of silicon and aluminum atoms in a structure, respectively. The numbers of oxygen and hydrogen atoms involved in each structure are determined in terms of  $x$  and  $y$ , based on the structure size and type. For cages, the presence of cation ( $M$ ) is also considered (eqn. 4), where  $i$  indicates the presence of a cation (1 if a cation exists and 0 otherwise) and  $z$  is the valence of the cation (+1 for Na and K, and +2 for Ca). Note that the formation Gibbs free energy is normalized by the number of T (tetrahedral, Si and Al) units with  $T = x + y$ , to eliminate exergonicity arising from different system sizes (i.e. we used an intensive form of free energy based on the number of T). The formation electronic energy and entropy are calculated in the same way by replacing  $G$  by  $E$  and  $S$  in equations (1-4), respectively.

### 3. Zeolitic Systems

Among various subunits of zeolite structures (e.g., soluble units, SBUs, and CBUs), we selected three families of species to study: monocycles, multicycles, and cages. Table 1 shows the four smallest structures in each family with graphical representations and names. The full list of the investigated species is available in the Supporting Information (Tables S1 – S6). Monocycles are cyclic structures composed of 3 or more T atoms, investigated up to dodecamer (12 T units). Each structure is named  $n$ MR for convenience ( $n$  = number of T units, i.e.,  $x + y$  in equation 1, and MR stands for “membered ring”). Another type of structure is a multicycle, which is linked 4MR, resembling the most frequently found “chains” in zeolite topologies (dzc, dcc, or dsc)<sup>62</sup>. Multicycles are named mono-ring, di-ring, etc., depending on the number of 4MR found in each structure. Note that the smallest multicycle, mono-ring, is identical to a 4MR species. The largest multicyclic structure (penta-ring) is composed of 12 T units. The *branched* multicyclic structures are also considered as intermediates connecting two complete multicycles. Finally, cages are prismatic structures, which are characterized by base size, i.e., trigonal prism, tetragonal prism, and so on. The largest cage investigated is an octagonal prism (16 T units).

**Table 1.** Names and graphics of the selected structures of three different families of zeolite subunits (monocycles, multicycles, and cages).

<b>Monocycles</b>	<b>Name</b>	3MR	4MR	5MR	6MR
	<b>Structure</b>	 (3)	 (4)	 (5)	 (6)
	<b>Conventional name</b>	cyclic trimer	cyclic tetramer	cyclic pentamer	cyclic hexamer
	<b>SBU name</b>	3	4	.	6
	<b>CBU name</b>	.	.	.	.
<b>Multicycles</b>	<b>Name</b>	Mono-ring	Branched mono-ring	Di-ring	Branched di-ring
	<b>Structure</b>	 (4)	 (5)	 (6)	 (7)
	<b>Conventional name</b>	cyclic tetramer	substituted cyclic tetramer	bicyclic hexamer	.
	<b>SBU name</b>	4	4-1	4-2	.
	<b>CBU name</b>	.	.	.	.
<b>Cages</b>	<b>Name</b>	Trigonal prism	Tetragonal prism	Pentagonal prism	Hexagonal prism
	<b>Structure</b>	 (6)	 (8)	 (10)	 (12)
	<b>Conventional name</b>	prismatic hexamer	cubic octamer	.	.
	<b>SBU name</b>	.	4-4	.	6-6
	<b>CBU name</b>	d3r	d4r	d5r	d6r

“MR” in monocycles stands for “membered ring”. In graphical representations, each vertex and edge represents a T (tetrahedral, Si or Al) atom and oxygen bridge, respectively, with terminal non-bridging oxygen (as hydroxyls or water) being omitted. Numbers in parenthesis alongside graphics stand for the number of T atoms in the structures. Conventional names of structures and SBU and CBU classifications<sup>62</sup> are given for reference (dots represent non-existing name convention). The full lists of the investigated species can be found in the Supporting Information with their optimized molecular structures (Tables S1 – S6).



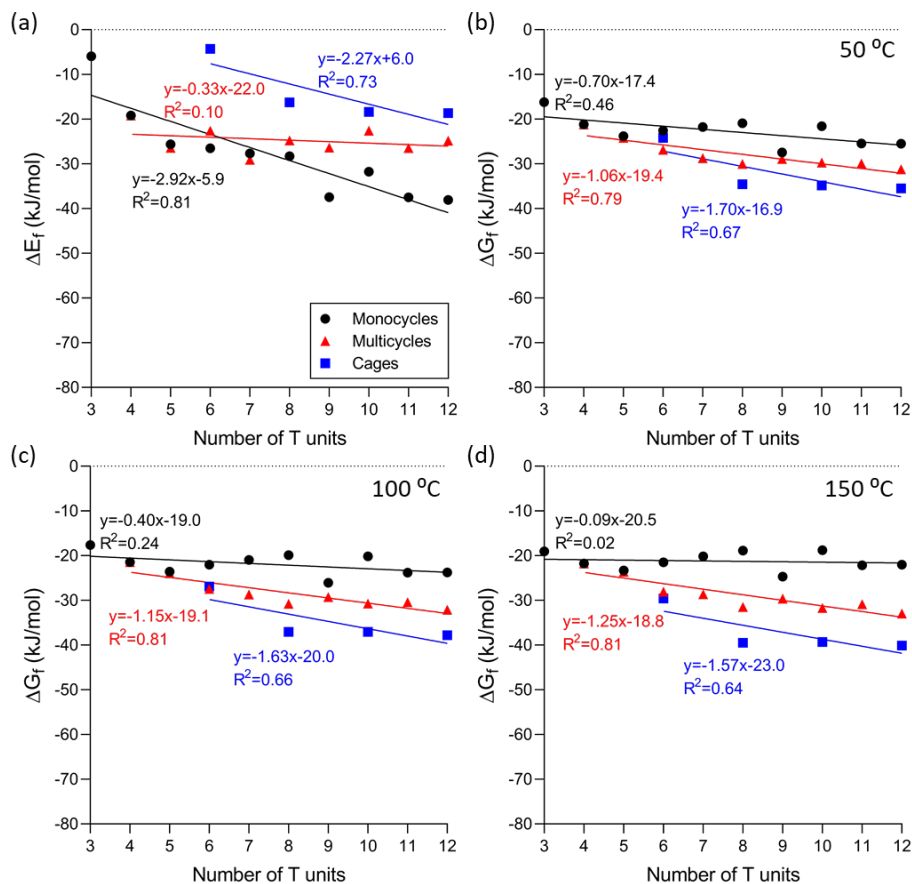
## 4. Results and Discussion

### 4.1. Structure and temperature effects

(1) *Pure-silicate system.* For pure-silicate species, we first study the dependence of formation energy on structure type and temperature in a cation-free environment. Figure 1 shows the formation electronic energies and Gibbs free energies of three different types of structures up to the 12 T-unit size. In terms of electronic energy (Figure 1(a)), monocycles compete with multicycles up to  $T=8$  (i.e., 8MR and tri-ring) whereupon monocycles become more favorable, while cages of all sizes show far less negative formation energy. Also, size effects are significant in monocycles, i.e., they prefer to form larger rings, whereas all multicycles and cages larger than trigonal prism do not show a significant size dependence. Conversely, trends change drastically in the formation Gibbs free energies when one accounts for temperature and entropic effects. At 50 °C (Figure 1(b)), cage formation becomes the most exergonic for all sizes except the smallest (trigonal prism), with progressively lower thermodynamic stability for multicycles and monocycles. In addition, multicycles show a clear size dependence favoring larger species, whereas the  $\Delta G_f$  of monocycles does not have a strong dependence on size. Increasing system temperature (50 °C  $\rightarrow$  150 °C) amplifies these differences such that the  $\Delta G_f$  of monocycles become size-independent, whereas the cage formation becomes increasingly exergonic at 150 °C. Hence, under typical zeolite synthesis (hydrothermal) conditions, silicate species prefer to exist in a more condensed form, which aligns well with experimental observations of a relatively high concentration of condensed silicates in solution<sup>12, 63</sup>. It is worth noting that there is no thermodynamic driving force for silicate cages to grow larger than a tetragonal prism as seen by the nearly identical formation Gibbs free energies from tetragonal to hexagonal prisms. This may explain the abundance of tetragonal prisms in silicate solutions under some experimental setups<sup>25, 63</sup> and final topologies<sup>62</sup>.

The changes in trends between  $\Delta E_f$  and  $\Delta G_f$  are attributed to entropic contributions since more condensed structures release more water molecules upon their formation. According to eqn.1-4, at the same number of T units ( $= x + y$ ), the coefficient associated with water is always larger in cages, followed by multicycles and monocycles. This results in significantly positive formation entropy for cages (Table S7), which negatively contributes (i.e., more exergonic) to the  $\Delta G_f$ . In contrast, the formation entropy is negative (i.e., endergonic contribution to  $\Delta G_f$ ) in monocycles

(except 3MR and 4MR), and insignificant in multicycles (Table S7). The temperature effects described here, which make the more condensed structures be thermodynamically favored, may explain why zeolite crystallization typically requires thermal treatment. We note that it was experimentally observed that the equilibrium among soluble silicate species shifts ~~is shifted~~ towards lower molecular weights at higher temperature<sup>6,64</sup>, which seems to contradict our findings. In fact, our results suggest that condensed species would be thermodynamically more stable than less condensed species at a higher temperature, regardless of how species populate in solution on observable time scales. In other words, polymerization kinetics, interactions between the species and structure-directing agents (SDAs), and pH effects should all be considered to explain experimental findings in aqueous silica solutions. This highlights the complexity of silicate solution chemistry, where formation thermodynamics may not dominate species growth and many factors contribute simultaneously. Nevertheless, our results clearly demonstrate that temperature significantly alters formation thermodynamics of zeolitic oligomers (due to entropic contributions), which in turn may lead to changes in precursor size, nucleation/growth rates, and reaction kinetics.

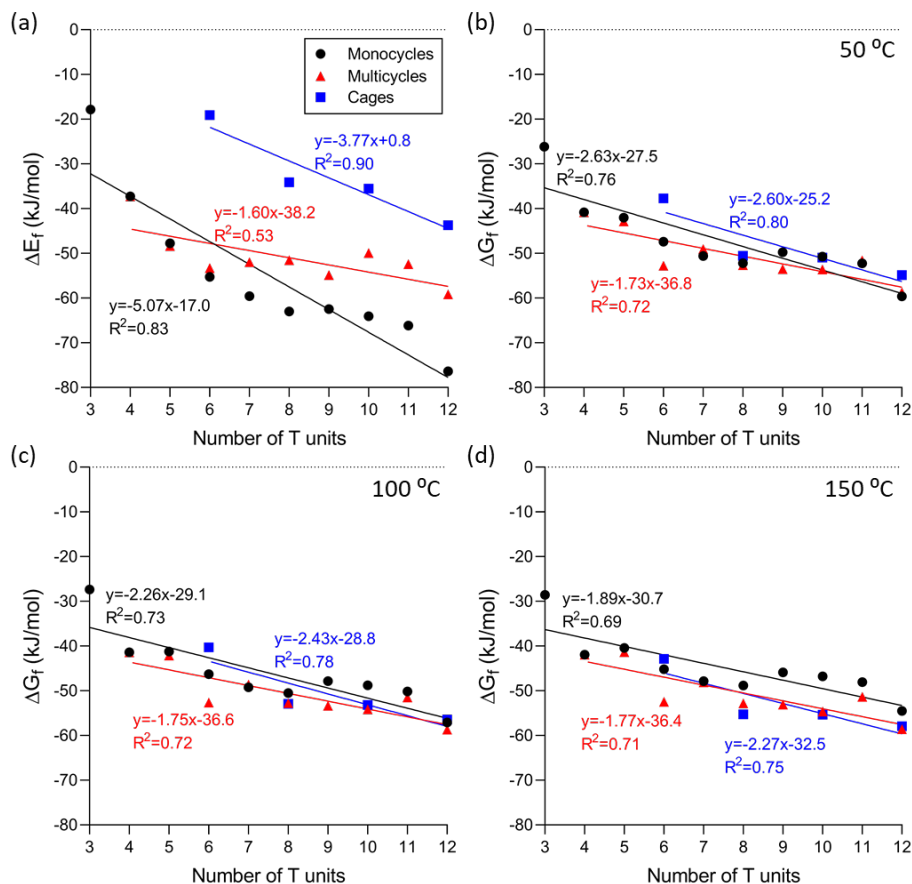


**Figure 1.** (a) Normalized formation electronic energies ( $\Delta E_f$ ) of pure-silicate structures, and their normalized formation Gibbs free energies ( $\Delta G_f$ ) determined at (b) 50 °C, (c) 100 °C, and (d) 150 °C. Fitted lines (determined by least square regression) serve as a guide to the eye for formation energy trends as a function of the structure size.

(2) *Aluminosilicate system.* Here, we repeat the same calculations as above (formation electronic/Gibbs free energies of 3 families of species) for aluminosilicate structures, where the maximum possible number of aluminum atoms are included in the framework ( $\text{Si}/\text{Al} \approx 1$ ), obeying Löwenstein's rule<sup>65</sup> (i.e., there are no Al-O-Al bridges). Monocycles and multicycles composed of an even number of T units have a Si/Al ratio of unity, while the other mono/multicycles have  $\text{Si}/\text{Al} > 1$ . For instance, a 3MR species has two Si and one Al ( $\text{Si}/\text{Al} = 2$ ), and a 5MR has 3 Si and 2 Al ( $\text{Si}/\text{Al} = 1.5$ ). Likewise, cages with an even-numbered base (tetragonal, hexagonal, and octagonal prisms) have  $\text{Si}/\text{Al} = 1$ , while others have  $\text{Si}/\text{Al} > 1$ . Using the lowest possible Si/Al ratio facilitates the identification of aluminum effects across different types of structures. It should be noted that

aluminosilicate multicycle and cage structures are not major species in solution. While Al-containing soluble species have been detected using NMR techniques, which include 3MR, 4MR, trigonal prism, and tetragonal prism, none of them contains more than two aluminum atoms<sup>26, 27, 66-69</sup>. Furthermore, those species are not abundant nor active enough to significantly contribute to zeolite crystal formation; rather, unstable and reactive small species (2-4 T units) are likely to take part in zeolite growth<sup>26, 69</sup>. Therefore, while the results shown below are not directly applicable to aluminosilicate solution chemistry, they are meaningful within the context of the thermodynamic stability of independent species and possibly crystals.

The inclusion of aluminum significantly alters formation energies compared to pure-silica structures, as shown in Figure 2. Aluminum enhances formation thermodynamics regardless of structure type and size and increases the size-dependency (more negative slopes). The formation electronic energy exhibits a similar trend as for silicates (more negative in the order of monocycles > multicycles > cages), but the energy difference between different families becomes more significant in aluminosilicates. Hence, accounting for entropic contributions results in eliminating the thermodynamic preference among different structure types in terms of Gibbs free energy at 50 °C, instead of inverting the order as observed in pure silicates. The increase in temperature plays the same role as that observed in the pure-silicate system, i.e., monocycles and cages become less and more exergonic, respectively, with only minimal effects being observed in multicycles. However, the formation energy difference among the three families is minimal at any size, even at 150 °C. Therefore, the effects of aluminum on the formation energy of zeolitic species are two-fold: (1) enhancing exergonicity and size-dependency, and (2) eliminating dependence on the structure type.



**Figure 2.** (a) Normalized formation electronic formation energies ( $\Delta E_f$ ) of aluminosilicate structures ( $\text{Si}/\text{Al} \approx 1$ ), and their normalized formation Gibbs free energies ( $\Delta G_f$ ) determined at (b) 50 °C, (c) 100 °C, and (d) 150 °C.

The enhanced formation thermodynamics and size-dependence in the presence of aluminum may imply the thermodynamically favorable crystallization of aluminosilicates compared to the pure-silicates. Using DFT calculations, Freeman and coworkers<sup>31</sup> also reported the more favorable formation of aluminosilicate oligomers (number of T units  $\leq 4$ ) compared to silicates of the same size, where the most negative formation energy is achieved at the lowest possible Si/Al ratio (= 1). Likewise, Muraoka et al. showed that higher aluminum content increases the thermodynamic stability of zeolite topologies that normally have a low Si/Al ratio<sup>70</sup>. Herein, the effects of the Si/Al ratio are also demonstrated in the formation Gibbs free energies of the small aluminosilicate species. At all temperatures, the formation of 5MR ( $\text{Si}/\text{Al} = 1.5$ ) is not favored over 4MR ( $\text{Si}/\text{Al} = 1$ ) (Figure 2), which is against the overall tendency that the larger species show more negative

formation energies. Likewise, for multicycles, a branched mono-ring ( $\text{Si}/\text{Al} = 1.5$ ) shows similar formation exergonicity with mono-ring ( $\text{Si}/\text{Al} = 1$ ), and a branched di-ring ( $\text{Si}/\text{Al} = 1.33$ ) is less exergonic than a di-ring ( $\text{Si}/\text{Al} = 1$ ). Finally, a trigonal cage ( $\text{Si}/\text{Al} = 2$ ) is less favorable than a di-ring ( $\text{Si}/\text{Al} = 1$ ), which is against the other cages that showed similar  $\Delta G_f$  with the multicycles of the same size. Although we have not systematically investigated the effect of  $\text{Si}/\text{Al}$  ratio on formation thermodynamics, the above examples reveal the general trend that lower  $\text{Si}/\text{Al}$  ratios allow for greater formation exergonicity. For species larger than those mentioned above, the effects of  $\text{Si}/\text{Al}$  ratio are not pronounced since it does not vary significantly. In fact, low-temperature (i.e., room temperature) crystallization has been successful only for low-silica zeolites, including zeolite A<sup>71, 72</sup> ( $\text{Si}/\text{Al} = 1$ ), zeolite X ( $\text{Si}/\text{Al} = 1.14\text{-}1.20$ )<sup>73, 74</sup>, zeolite Y ( $\text{Si}/\text{Al} = 1.95\text{-}2.52$ )<sup>75</sup>, and EMT zeolite ( $\text{Si}/\text{Al} = 1.14$ )<sup>76</sup>, whereas highly siliceous zeolites typically require moderate to high temperature<sup>77-79</sup>. Therefore, we posit that aluminum has a crucial role in facilitating the crystallization of zeolites by introducing a thermodynamic driving force.

The second effect (i.e., no strong preference towards condensed aluminosilicates) indicates that the presence of aluminum results in generating a diverse pool of thermodynamically stable aluminosilicate structures. Table 2 shows structure information of some highly siliceous zeolites that can be hydrothermally synthesized in an alkaline media<sup>80</sup> and do not contain heteroatomic framework elements (i.e., elements besides Si and Al). Their framework densities, listed in units of  $T/1000 \text{ \AA}^3$ , are high ( $>17$ ) relative to all reported zeolites ( $13\text{-}21$ )<sup>57</sup>, whereas those of low-silica aluminosilicate zeolites have a wider range and can be as low as 13 (e.g., FAU and LTA). Our calculations combined with structural information presented in Table 2 collectively indicate that aluminum-based stabilization of a pool of different structures (besides cages) may enable the synthesis of more metastable and diverse topologies. Some frameworks contradict this argument; for instance, certain ITQ-family structures are purely siliceous zeolites with extra-large pores and relatively low framework density<sup>62</sup>. However, experimental factors for their synthesis (HF media with bulky OSDAs<sup>81, 82</sup> or pressure-induced phase transformations<sup>83</sup>) are far from conventional hydrothermal methods and not considered in our computation results. Overall, Figure 2 reveals the general tendency that aluminosilicates allow for greater framework diversity because of the strong stabilization effects of aluminum on the formation of various types of species (i.e., monocycles, multicycles and cages). This is contrary to what is observed on the purely siliceous species, which

show a strong thermodynamic preference towards highly condensed structures (i.e., cages) (Figure 1).

**Table 2.** Structural information of select highly siliceous zeolites.

Material (topology)	Si/Al ratio	Framework density* (T/1000 Å <sup>3</sup> )
ZSM-5 (MFI)	≥ 15 <sup>84, 85</sup>	18.4
ZSM-11 (MEL)	≥ 15 <sup>79, 86</sup>	17.4
ZSM-12 (MTW)	≥ 30 <sup>87</sup>	18.2
ZSM-22 and Theta-1 (TON)	≥ 25 <sup>88, 89</sup>	18.1
ZSM-23 and SSZ-32 (MTT)	≥ 20 <sup>90, 91</sup>	18.2
ZSM-48 (*MRE)	≥ 30 <sup>92</sup>	19.7

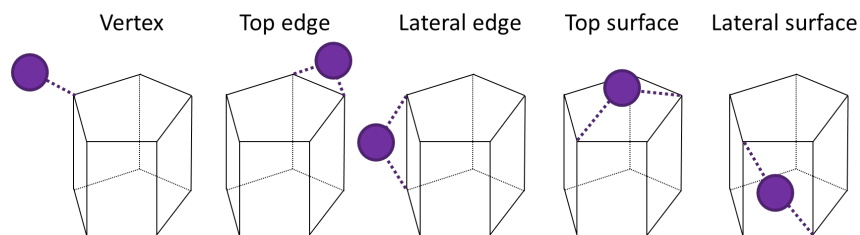
\*Data sourced from the International Zeolite Association<sup>62</sup>.

#### 4.2. Cages with alkali/alkaline earth metal cations

After we investigated the formation thermodynamics of pure-silicate and aluminosilicate cages, we systematically studied the effects of alkali and alkaline earth metal cations (i.e., Na<sup>+</sup>, K<sup>+</sup>, and Ca<sup>2+</sup>). These cations counterbalance the negatively charged cages, which emerge from either the highly alkaline synthesis environment or the presence of trivalent aluminum in tetrahedral framework positions. We focus on cages because they represent interactions between zeolite crystals and cations better than less condensed species (i.e., monocycles and multicycles). In addition, the formation of oligomers in the presence of cations has been investigated in detail with DFT calculations<sup>24, 30, 31</sup>.

(1) *External cations.* Since cages are 3-dimensional structures with internal volume, cations can be located either externally or internally. A cation can be placed in various external positions as depicted in Figure 3. As mentioned in the Computational Details section, cations are introduced to the system assuming a dehydration reaction between a zeolitic cage and cation hydroxide, which results in a charge-neutral species. Essentially, alkali metal cations replace one proton on either hydroxyl (on Si in pure-silicates) or water (on Al in aluminosilicates) from different positions of

the optimized cation-free cages. Likewise, two protons are removed to add a calcium cation. The vertex position represents that a cation is introduced taking the original position of the removed proton, resulting in a single terminal cation-oxygen pair. If a cation replaces a proton but interacts with another nearby terminal or framework oxygen simultaneously, the cation resides at an edge position. A surface position represents that a cation is not in the proximity of the terminal oxygen or hydroxyl (from which a proton is removed) but strongly interacts only with the framework oxygens. The cage structures with an external cation (including detailed info of cation placement) can be found in the Supporting Information (Table S3 and S4).



**Figure 3.** Possible external positions of cation associated with (alumino)silicate cages. Each vertex and edge in black represent a T atom and oxygen bridge, respectively, with terminal non-bridging oxygen (as hydroxyls or water) omitted. The purple sphere indicates a single cation. Note that there is no distinction between the top and side edges nor between the top and side surfaces in the tetragonal prism. The optimized molecular structures are available in Table S3 and S4.

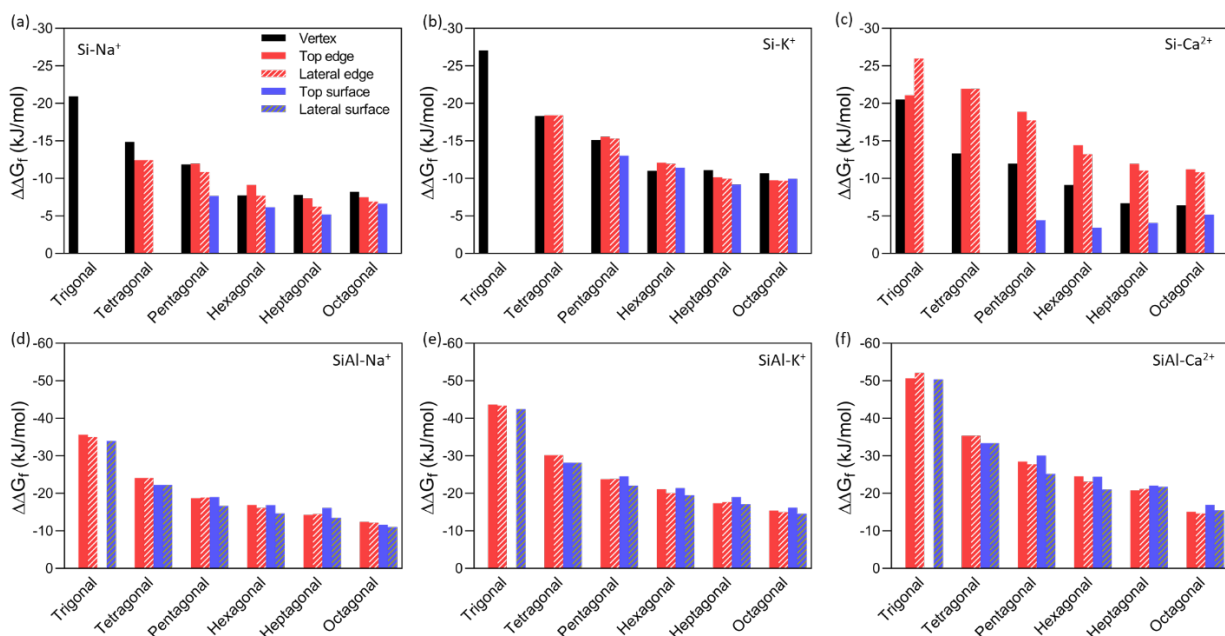
Figure 4 shows the relative Gibbs free energies of formation ( $\Delta\Delta G_f$ ) of cages with an external cation, which are calculated by equation (5):

$$\Delta\Delta G_f = \Delta G_f - \Delta G_f^{\text{ref}} \quad (5)$$

where  $\Delta G_f$  is the formation Gibbs free energy determined by equation (4) in the presence of cation ( $i = 1$ ), and  $\Delta G_f^{\text{ref}}$  is that of the corresponding cation-free structure ( $i = 0$ ). Overall, external cations enhance exergonicity of cage formation regardless of cage size and cation type, which indicates that interactions between (alumino)silicate species and cations can facilitate zeolite formation. Thermodynamic stabilization by cations is the primary reason why zeolite



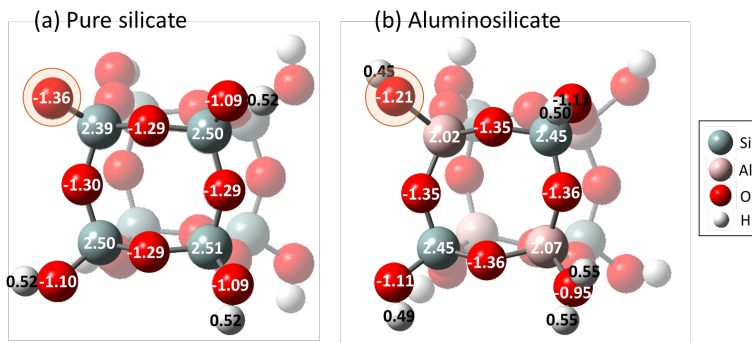
nucleation/growth always occurs in the presence of cations<sup>20</sup>. Also, it is consistently observed that cation effects are more significant in smaller cages. Considering that the calculated formation energies are normalized by the number of T units in cages, the decrease in exergonicity of  $\Delta\Delta G_f$  with size indicates that cation effects *per T unit* decrease with size, rather than interactions between cation and cages diminish with cage size.



**Figure 4.** Relative formation Gibbs free energies ( $\Delta\Delta G_f$ ) of silicate (a-c) and aluminosilicate (Si/Al  $\approx$  1, d-f) cages with an alkali or alkaline metal cation ( $\text{Na}^+$ ,  $\text{K}^+$ , or  $\text{Ca}^{2+}$ ) located at an external position (vertex, top edge, lateral edge, top surface, or lateral surface). The Gibbs free energies are determined at 100 °C. Missing data points indicate that the cation at the corresponding position moves to another position during optimization.

For pure-silicate cages with alkali metal cations (Figure 4(a) and (b)), the vertex position is equally or more favorable compared with top/lateral edge positions. On the other hand, the divalent cation ( $\text{Ca}^{2+}$ ) has a strong thermodynamic preference for edge positions rather than vertex positions (Figure 4(c)), which is attributed to the cation valence. The interactions between the monovalent cation and cage are maximized with the presence of one cation-oxygen pair, and additional

interactions do not significantly contribute to formation thermodynamics. In contrast, calcium can strongly interact with two negatively charged terminal oxygen atoms simultaneously, i.e., edge positions. Compared to edge/vertex positions, cations located on the surface have less impact on the formation thermodynamics of pure-silicate cages. Surfaces that are smaller than 5MR (i.e., the top surface of the trigonal and tetragonal cages, and the lateral surfaces of cages of any size) are unable to hold a cation (the cation initially located at those locations moved to nearby vertex or edge during optimization). Furthermore, larger rings (top surfaces of pentagonal and larger cages) show less negative  $\Delta\Delta G_f$  compared to vertex/edge positions. Figure 5(a) shows the charge distribution on the surface of single negatively charged silicate tetragonal prisms calculated with Natural Bond Orbital (NBO) analysis<sup>93</sup> as implemented in Gaussian 09, at the same level of theory (M062X/6-311g(d,p)). The terminal oxygen is the most negatively charged (-1.36) because of proton removal, which is therefore capable of strong interactions with a cation. Although framework oxygen atoms are also negatively charged (around -1.29), highly positive framework silicon atoms ( $\geq 2.39$ ) prevent strong attraction between the cation and the cage body. As ring size increases, framework oxygen atoms become more accessible to cations, but surface positions consistently show the least negative  $\Delta\Delta G_f$  (Figure 4(a-c)), with only one exception at the largest ring with  $K^+$  (top surface of the octagonal prism, Figure 4(b)). The charge distribution calculated with the NBO method aligns well with reported values for the BEA zeolite structure<sup>94</sup> determined by GGA-PBE exchange-correlation functional, coupled with the Iterative Hirshfeld or Density Derived Electrostatic and Chemical charge method: +2.55 to +2.62 for Si and -1.26 to -1.31 for O. Additionally, the authors identified the Extended Charge Equilibration semi-empirical method showing very good agreement with the DFT calculated charges: +2.53 for Si and -1.26 for O. In comparison, most molecular dynamics studies have used atomic charges (Si: +1.6 to +2.1, Al: +1.2 to +1.8, and O: -0.8 to -1.2), which are smaller in magnitude than the values reported here to account for the framework-cation or framework-adsorbate Coulombic interactions<sup>95-98</sup>. Hence, the atomic charge density determined at the high level of theory in this work may be used in future studies for more accurate description of electrostatic interactions.



**Figure 5.** Atomic charges on one plane of the cation-free pure-silicate (a) and aluminosilicate (b) tetragonal prisms, which possess a -1 overall charge by removing one terminal proton (left top, highlighted by orange circle) from the optimized neutral species. The atomic charge is calculated by Natural Bond Orbital analysis<sup>93</sup>.

As expected, Figure 4(d-f) reveals that aluminosilicate cages interact with cations very differently compared to pure-silicates, which is attributed to the different charge distribution on the framework atoms (Figure 5(b)). The negative charge of the terminal hydroxyl on aluminum (generated by removing one proton from terminal water; -1.21) is smaller in magnitude than that of the terminal oxygen of pure-silicates (-1.36), whereas framework oxygen atoms in aluminosilicates are more negatively charged (-1.35 or -1.36) than those in silicates (-1.29 or -1.30). At the same time, aluminum is less positively charged than silicon. These differences strongly favor cationic attraction on edge positions as they allow cations to interact with terminal and framework oxygen simultaneously. As a result, a cation located at a vertex position always moves to edge/surface positions during geometry optimization, as indicated by the missing data for the vertex position (Figure 4 (d-f)). Moreover, the top surface positions of cages larger than tetragonal prisms ( $\geq 5\text{MR}$ ) attract cations as strongly as edges because the cations can strongly interact with framework oxygens. In fact, framework oxygen atoms are more negatively charged than the oxygen of the terminal hydroxyl (-1.35 or -1.36 vs. -1.21, Figure 5(b)). This indicates that cation – cage interactions are less localized in the aluminosilicate system compared to the pure-silicates. This phenomenon is putatively due to the presence of aluminum changing the charge distribution of multiple neighboring atoms, especially since the investigated systems possess high aluminum content (i.e., aluminum is spread throughout the cages).

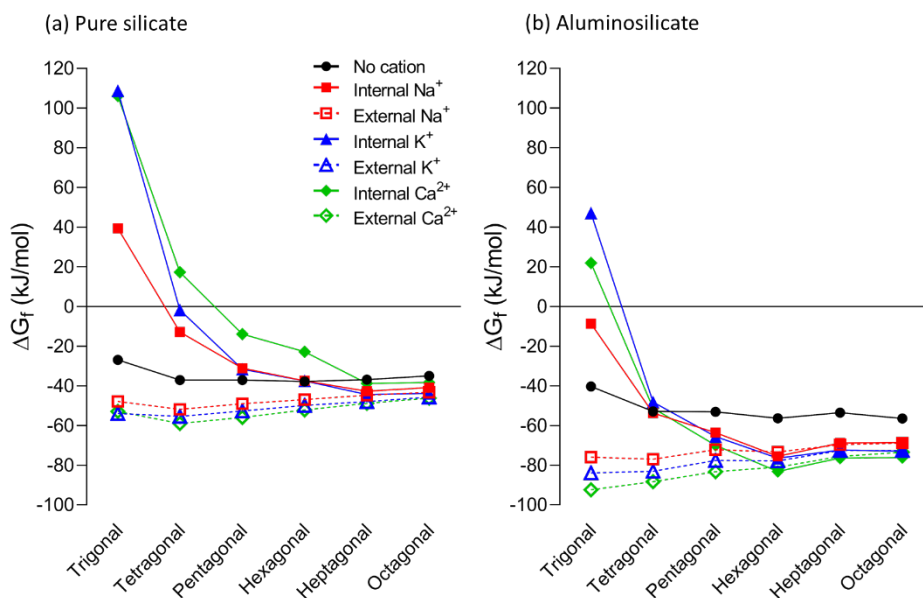
The differences in the effects of cations are also worth noting. Essentially, monovalent cations ( $\text{Na}^+$  and  $\text{K}^+$ ) show similar trends of  $\Delta\Delta G_f$  with cage size and cation position in each system (Figure 4(a) and (b) for pure-silicates and Figure 4(d) and (e) for aluminosilicates). However, the effects of potassium are consistently stronger (more negative  $\Delta\Delta G_f$ ) than sodium. This does not necessarily indicate that potassium more effectively directs the same type of crystal structures as sodium. Instead, the different formation thermodynamics can significantly alter the crystallization kinetics and therefore final zeolite topologies. Indeed, it has been well demonstrated that different alkali metal cations can have various structure-directing effects. In the pioneering work of Barrer et al. in the 1950s<sup>99, 100</sup>, it was found that aluminosilicate gels with identical chemical compositions except for alkali metal cation selection ( $M_2\text{O}-\text{Al}_2\text{O}_3-n\text{SiO}_2$ , where  $M = \text{Na}$  or  $\text{K}$  and  $1 < n < 12$ ) can result in either the same or different types of zeolite/aluminosilicate minerals, depending on the hydrothermal synthesis conditions. Further, they revealed that the  $\text{Na}^+/\text{K}^+$  ratio is a key factor to determine the product crystals when both cations are used together, which demonstrated that  $\text{Na}^+$  and  $\text{K}^+$  can play different structure-directing roles<sup>1</sup>. Likewise, Iwama et al.<sup>101</sup> showed that the controlled addition of potassium could change the selectivity of FAU-type zeolite over LTA by altering the aluminosilicate precursor assembly. Tendeloo et al.<sup>56</sup> synthesized various zeolite crystals (ABW, CHA, MER, and ANA) via interzeolite transformation from zeolite Y using different alkali metals. Moreover, the distinct roles of alkali metal cations ( $\text{Na}^+$ ,  $\text{K}^+$ , and  $\text{Cs}^+$ ) during the synthesis of CHA nanocrystals were identified by Ghojavand et al.<sup>102</sup>, where a mixture of the cations was used. Rimer et al. showed that the zeolite synthesis phase diagram constructed with  $\text{K}^+$  is completely different from that with  $\text{Na}^+$ , which demonstrates the significant effect of the cations in altering crystallization kinetics<sup>103, 104</sup>.

The effects of calcium on the formation energy of (alumino)silicates are different from those of monovalent cations (Figure 4(c) and (f) for pure-silicates and aluminosilicates, respectively). These effects can be attributed to a higher valence state (+2 rather than +1). In the aluminosilicate system, the trends of  $\Delta\Delta G_f$  with the cage size and cation position are similar for all cations, but calcium consistently shows the most negative  $\Delta\Delta G_f$  (Figure 4(d-f)). This is because the higher-valent cation has stronger electrostatic interactions with terminal/framework oxygen atoms. Interestingly, in the pure-silicate system, we show that the dependence of  $\Delta\Delta G_f$  on cation position is significantly different in calcium compared to the alkali metals, where the edge positions surpass the vertex in exergonicity. These observations indicate that the divalent cation can play a

considerably different structure-directing role than those of monovalent cations. Compared with alkali metal cations, relatively little attention has been devoted to exploring the possibilities of altering crystallization pathways using divalent cations; however, divalent cations such as  $\text{Ca}^{2+}$  and  $\text{Mg}^{2+}$  are present in a number of naturally-forming zeolites (e.g., GIS<sup>105</sup>, CHA<sup>106</sup>, and FER<sup>107</sup>), and it has been shown that introducing divalent cations into zeolite growth mixture has a potential to alter zeolite crystallization pathways. For example, Liang et al. recently observed that introducing  $\text{Sr}^{2+}$  in K-CHA growth mixtures can lead to a dramatic reduction in CHA crystallization time<sup>108</sup>. Similarly, it has been demonstrated that  $\text{Mg}^{2+}$  can promote zeolite \*BEA<sup>109</sup>. Collectively, previous studies have shown that the use of different cations can direct structure and/or accelerate zeolite kinetics, and our findings suggest that this may be attributed to electrostatic effects on the formation thermodynamics of small zeolitic species, which stem from the difference in cation size and charge. Although our study addresses formation thermodynamics of small zeolitic structures, it should be noted that changes in reaction free energies can affect kinetics of zeolite crystallization through the well-known Brønsted-Evans-Polanyi relationships<sup>110</sup>, which have been shown to play a role in both nucleation and growth of nanoparticles<sup>111</sup>.

(2) *Internal cations.* In addition to external positions, we investigated the thermodynamic effects of cations occupying the center of the cage. The formation Gibbs free energies of cages confining cations are shown in Figure 6, along with those of cation-free cages and cages with the external cations at the most stable positions (shown in Figure 4). Interestingly, the pure-silicate trigonal prism with an internal cation shows significantly endergonic formation energies (Figure 6(a)). Additionally, the formation of pure-silicate tetragonal and pentagonal prisms (for all cations) and the hexagonal prism (for calcium) is less favored than the corresponding cation-free cages. In contrast, larger silicate cages (heptagonal prism with alkali metal cations and octagonal prism with all cations) show enhanced formation exergonicity relative to the cation-free cages (black), which indicates the cage size should be sufficiently large for an internal cation to provide thermodynamic stabilization. However, the effects of internal cations on aluminosilicate cages are significantly different from those on pure-silicate cages (Figure 6(b)). Although the smallest (trigonal) cage is endergonic ( $\text{K}^+$  and  $\text{Ca}^{2+}$ ) or nearly thermoneutral ( $\text{Na}^+$ ) in formation with an internal cation, tetragonal prisms with an internal cation show the same exergonicity as cation-free cages, and

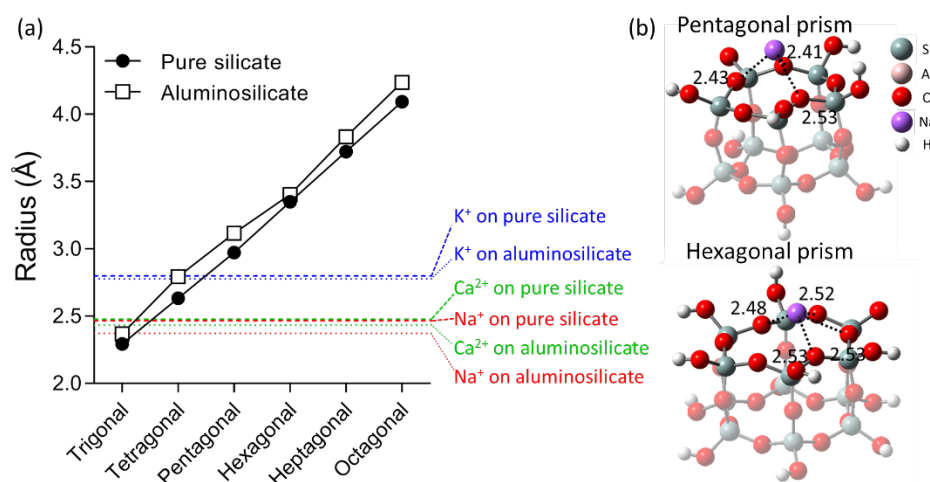
larger cages show significantly more exergonic formation energies. For pentagonal prisms and larger cages, there is no noticeable difference between the net effects of internal vs. external cations.



**Figure 6.** Normalized formation Gibbs free energies ( $\Delta G_f$ ) of (a) silicate and (b) aluminosilicate ( $\text{Si}/\text{Al} \approx 1$ ) cages with and without an alkali or alkaline metal cation ( $\text{Na}^+$ ,  $\text{K}^+$ , or  $\text{Ca}^{2+}$ ) at internal and external positions. The external cations are located at positions that exhibit the most exergonic formation energy (see Figure 4). The Gibbs free energies are determined at 100 °C.

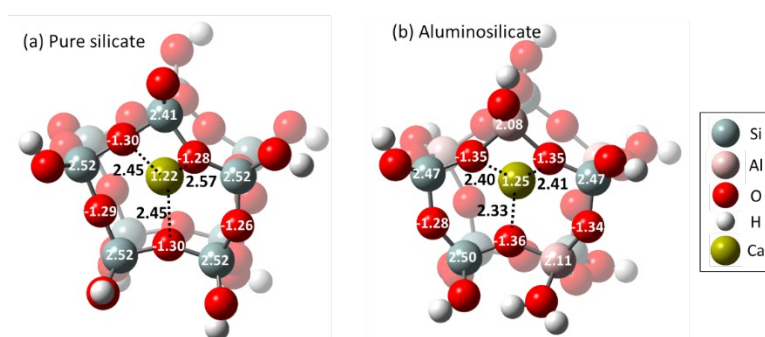
The observations described above clearly demonstrate the interplay of electrostatic interactions and steric effects between the different cages and cations. As discussed, a cation can have attractive interactions with framework oxygen atoms because of their negative charge. The cages that are optimized in the presence of cations at the external top surface position can provide the optimal distance information between cation and framework oxygen since there are no confinement effects. Figure 7 shows the cage radii, which are determined as average Euclidean distances from the geometric center of framework oxygen atoms to each oxygen in the optimized cation-free cages. Also, average distances between the cation at the top surface and framework oxygen atoms that attractively interact with each cation are shown for comparison (dashed and dotted lines in Figure 7, for pure-silicates and aluminosilicates, respectively). The stable cation-framework oxygen

distances are longer than the radius of the trigonal prisms, which indicates that the trigonal prisms impose strong steric hindrances and are thus destabilized. Pure-silicate tetragonal prisms also do not have sufficient space to confine potassium, while the radius of the aluminosilicate tetragonal prism is comparable to the potassium-oxygen distance. Therefore, all cages larger than a tetragonal prism are not likely to impose steric hindrance to any internal cation, which is the case for the aluminosilicate systems, as seen in Figure 6(b). In contrast, there are many pure-silicate cages that do not confine cations with strong favorability despite their sufficiently large space (i.e., pentagonal and hexagonal prisms for all cations, and heptagonal prism for calcium), and this can be attributed to the weak attractive interactions between the cage body and the cation (compared to aluminosilicate species). The discussion herein is clearly displayed in the charge density and optimized geometry of pentagonal prisms confining calcium, as shown in Figure 8. The electrostatic cation-cage interactions are stronger in the presence of aluminum due to the more negatively charged oxygen atoms, which is reflected in the shorter cation-oxygen distances (Figure 7(a) and Figure 8). These differences lead to the opposite effects from calcium confinement on the formation of the pure-silicate and aluminosilicate pentagonal cages, which are destabilizing and stabilizing, respectively (Figure 6).



**Figure 7.** (a) Radii of pure-silicate and aluminosilicate (Si/Al  $\approx$  1) cages (solid lines with symbols) and optimal distances between (external) cation and framework oxygens (dashed lines for pure-silicates and

dotted lines for aluminosilicates) (both in Å). On a cation-free cage, a geometric center between the framework oxygens is defined, with the average distance from the center to the framework oxygens defining the cage radius. The optimal cation-framework oxygen distances are determined on the cages optimized in the presence of a cation at the top surface position. The framework oxygens that are closely bound to the cation are selected, and the distances between the cation and framework oxygens are averaged. (b) Optimized molecular structures of pure-silicate cages in the presence of sodium on the top surface, along with the distances between sodium and the selected framework oxygens (in Å).



**Figure 8.** Charge of framework atoms on a base of (a) pure-silicate and (b) aluminosilicate pentagonal prisms that confine calcium cation, as well as distances between cation and framework oxygen atoms (in Å). Atomic charges are calculated by Natural Bond Orbital analysis.

The thermodynamic understanding of the relationship between cage and cation reveals potential roles and limitations of cations in zeolite formation chemistry. We show that pure-silicate cages interact with alkali or alkaline earth metal cations primarily at external vertex/edge positions unless the cage is sufficiently large ( $>$  hexagonal prism) to allow framework oxygen to confine cations. Moreover, the cations at an external location consistently show stronger stabilizing effects to pure-silicate cages compared to internal cations. These indicate that attractive interactions between pure-silicate cages and small inorganic cations (compared with bulky OSDAs) are extremely localized, which may adversely affect the stability of cages. This supports the experimental observation that the presence of alkali metal cations ( $\text{Na}^+$ ) changes the stabilization of silicate cage species in solution<sup>64</sup>. On the other hand, aluminosilicate cages are shown to attractively interact



with the cations, as seen by equally exergonic cage formation with internal and external cations (for cages > tetragonal prism). These results corroborate the fact that the formation of pure-silicate species is only viable with bulky, hydrophobic, organic cations (e.g., tetraethylammonium cation (TEA<sup>+</sup>) and tetramethylammonium cation (TMA<sup>+</sup>)<sup>63</sup>), whereas aluminosilicate zeolites can be synthesized in the presence of alkali metal cations<sup>20</sup>. For the crystallization of siliceous zeolites, the role of alkali metal cations has been limited to facilitating the reaction in the presence of OSDAs<sup>112</sup> or seed crystals<sup>113</sup>. Our results demonstrate that the key of OSDA-free synthesis of siliceous zeolites lies in enhancing attractive electrostatic interactions between the framework atoms and cation (for example, by introducing heteroatoms into the framework) or exploring bulkier inorganic cations (i.e., less charge density). Further, we posit that novel combinations of OSDAs and inorganic cations can be used to synthesize novel zeolite frameworks by stabilizing cages and structures that are not energetically favorable in conventional zeolite syntheses. Of more than 300,000 theoretically predicted zeolite frameworks<sup>114</sup>, only a small number (~250) have been realized experimentally, and it has been suggested that unique cation pairings are one method for designing previously unrealized architectures<sup>115</sup>.

## Conclusions

In this work, we studied the formation thermodynamics of a wide range of zeolitic species by applying density functional theory calculations. For purely siliceous and aluminosilicate (Si/Al  $\approx$  1) complexes, we systematically investigated the dependence of formation energy on structure type, structure size, temperature, and the presence of alkali or alkaline earth metal cations (Na<sup>+</sup>, K<sup>+</sup>, and Ca<sup>2+</sup>). It was found that the most condensed form of pure-silicate species, i.e., prismatic cages, show the highest exergonic formation, followed by multicyclic structures (linked 4-membered rings) and monocyclic structures (simple rings), since the higher degree of condensation favors entropic contributions, leading to more negative formation Gibbs free energy (i.e., more exergonic). As the entropic contribution to the Gibbs free energy is proportional to temperature, the formation preference of condensed structures increases with temperature. Conversely, investigation of aluminum-rich structures reveals significantly different trends. The thermodynamic preference among the three types of species almost vanishes with temperature (50-150 °C), imposing the formation of complexes with high structural diversity, while a size-

dependence appears, favoring larger structures. At the same time, it was found that the formation Gibbs free energy of aluminosilicate structures is significantly more exergonic than pure-silicates. These findings consistently support the abundance of aluminum-rich natural and synthetic zeolites. The effects of cations on formation thermodynamics of cages were found to depend highly on cation charge and size, cage size, and the presence of aluminum, which alters electrostatic interactions. In the case of pure-silicate cages, a terminal oxygen atom (resulting from the proton on terminal hydroxyl group being exchanged with cation) is more negatively charged than framework oxygens, so that the optimal location of a cation is an external vertex or edge, instead of being in proximity of framework atoms (i.e., surfaces) or inside cages. In contrast, framework aluminum and oxygen atoms in aluminosilicate cages (with high aluminum content) are less positively and more negatively charged, respectively, compared to silicon and oxygen in the pure-silicate cages. Therefore, for aluminosilicates, cations can strongly interact with the cage body (at surface or inside of cage) only if cages are sufficiently large to overcome steric hindrance. This supports experimental observations that alkali metal cations can direct growth of many aluminosilicate zeolites, whereas highly siliceous zeolites require the use of bulky organic cations or seed crystals.

Overall, the formation thermodynamics provided herein can potentially guide experimental efforts for discovering more effective synthetic methods of zeolite crystals. Moreover, our detailed study of structurally diverse zeolitic oligomers can provide insights into controlling specific zeolite synthesis pathways, including prenucleation pathways and interzeolite transformations. At the same time, a further theoretical investigation is required to address the effects of experimental factors that are omitted in the current work, e.g., alkaline pH conditions, explicit solvent, kinetics, and types of raw materials, for a more accurate description of zeolitic species growth. In particular, efforts using explicit solvation environments to more precisely capture cation effects on zeolite crystallization processes, as well as the role of water molecules on the reaction kinetics can be instrumental to unravel zeolite growth.

### **Author Contributions**

The project was conceived by JDR, JJN, RKM, and GM. All density functional theory calculations in this work were performed by SH. The original draft of the manuscript was prepared by SH and

GM, with feedback from AJM and JDR. All authors contributed to editing and finalizing the manuscript.

### Conflicts of Interest

The authors declare no conflict of interest.

### Acknowledgements

This work was supported by the US Department of Energy's Nuclear Energy University Programs (NEUP) under Award 18-15496. The authors would like to acknowledge computational support from the Center for Research Computing at the University of Pittsburgh.

### References

1. R. M. Barrer, J. W. Baynham, F. W. Bultitude and W. M. Meier, *Journal of the Chemical Society*, 1959, 195-208.
2. W. C. Beard, in *Molecular Sieves*, eds. W. M. Meier and J. B. Uytterhoeven, ACS Publications, Washington DC, 1973, vol. 121, ch. 13, pp. 162-168.
3. R. K. Harris and C. T. G. Knight, *Journal of Molecular Structure*, 1982, **78**, 273-278.
4. R. K. Harris and C. T. G. Knight, *Journal of the Chemical Society, Faraday Transactions 2: Molecular and Chemical Physics*, 1983, **79**, 1525-1538.
5. P. K. Dutta and D. C. Shieh, *Journal of Raman Spectroscopy*, 1985, **16**, 312-314.
6. S. D. Kinrade and T. W. Swaddle, *Inorganic Chemistry*, 1988, **27**, 4253-4259.
7. P. Bodart, J. B. Nagy, Z. Gabelica and E. G. Derouane, *Journal de Chimie Physique*, 1986, **83**, 777-790.
8. C. E. A. Kirschhock, R. Ravishankar, F. Verspeurt, P. J. Grobet, P. A. Jacobs and J. A. Martens, *The Journal of Physical Chemistry B*, 1999, **103**, 4965-4971.
9. R. Ravishankar, C. E. A. Kirschhock, P.-P. Knops-Gerrits, E. J. P. Feijen, P. J. Grobet, P. Vanoppen, F. C. De Schryver, G. Miehe, H. Fuess and B. J. Schoeman, *The Journal of Physical Chemistry B*, 1999, **103**, 4960-4964.
10. C. E. A. Kirschhock, S. P. B. Kremer, P. J. Grobet, P. A. Jacobs and J. A. Martens, *The Journal of Physical Chemistry B*, 2002, **106**, 4897-4900.
11. C. J. Y. Houssin, C. E. A. Kirschhock, P. C. M. M. Magusin, B. L. Mojet, P. J. Grobet, P. A. Jacobs, J. A. Martens and R. A. van Santen, *Physical Chemistry Chemical Physics*, 2003, **5**, 3518-3524.
12. C. T. G. Knight, *Zeolites*, 1990, **10**, 140-144.
13. D. D. Kragten, J. M. Fedeyko, K. R. Sawant, J. D. Rimer, D. G. Vlachos, R. F. Lobo and M. Tsapatsis, *The Journal of Physical Chemistry B*, 2003, **107**, 10006-10016.
14. C. T. G. Knight and S. D. Kinrade, *The Journal of Physical Chemistry B*, 2002, **106**, 3329-3332.

15. C. T. G. Knight, J. Wang and S. D. Kinrade, *Physical Chemistry Chemical Physics*, 2006, **8**, 3099-3103.
16. C. T. G. Knight, R. J. Balec and S. D. Kinrade, *Angewandte Chemie*, 2007, **119**, 8296-8300.
17. G. T. Kerr, *The Journal of Physical Chemistry*, 1966, **70**, 1047-1050.
18. S. P. Zhdanov, in *Molecular Sieve Zeolites-I*, eds. E. M. Flanigen and L. B. Sand, ACS Publications, Washington DC, 1971, vol. 101, ch. 2, pp. 20-43.
19. C. D. Chang and A. T. Bell, *Catalysis Letters*, 1991, **8**, 305-316.
20. D. W. Breck, *Zeolite Molecular Sieves: Structure, Chemistry and Use*, John Wiley & Sons, New York, 1974.
21. S. L. Burkett and M. E. Davis, *The Journal of Physical Chemistry*, 1994, **98**, 4647-4653.
22. P. Norby, *Current Opinion in Colloid & Interface Science*, 2006, **11**, 118-125.
23. S. Mintova, N. H. Olson and T. Bein, *Angewandte Chemie International Edition*, 1999, **38**, 3201-3204.
24. K. Selvaraj and R. Kurian, *Microporous and Mesoporous Materials*, 2009, **122**, 105-113.
25. S. D. Kinrade, C. T. G. Knight, D. L. Pole and R. T. Syvitski, *Inorganic Chemistry*, 1998, **37**, 4272-4277.
26. A. Thangaraj and R. Kumar, *Zeolites*, 1990, **10**, 117-120.
27. A. V. McCormick, A. T. Bell and C. J. Radke, *The Journal of Physical Chemistry*, 1989, **93**, 1741-1744.
28. M. J. Mora-Fonz, C. R. A. Catlow and D. W. Lewis, *Angewandte Chemie*, 2005, **117**, 3142-3146.
29. T. T. Trinh, A. P. J. Jansen and R. A. van Santen, *The Journal of Physical Chemistry B*, 2006, **110**, 23099-23106.
30. C. E. White, J. L. Provis, G. J. Kearley, D. P. Riley and J. S. J. Van Deventer, *Dalton Transactions*, 2011, **40**, 1348-1355.
31. E. E. Freeman, J. J. Neeway, R. K. Motkuri, J. D. Rimer and G. Mpourmpakis, *AIChE Journal*, 2020, **66**, e17107.
32. X.-Q. Zhang, T. T. Trinh, R. A. van Santen and A. P. J. Jansen, *Journal of the American Chemical Society*, 2011, **133**, 6613-6625.
33. X.-Q. Zhang, R. A. van Santen and A. P. J. Jansen, *Physical Chemistry Chemical Physics*, 2012, **14**, 11969-11973.
34. M. Moqadam, E. Riccardi, T. T. Trinh, A. Lervik and T. S. van Erp, *Physical Chemistry Chemical Physics*, 2017, **19**, 13361-13371.
35. V. A. Blatov, G. D. Ilyushin and D. M. Proserpio, *Chemistry of Materials*, 2013, **25**, 412-424.
36. E. D. Kuznetsova, O. A. Blatova and V. A. Blatov, *Chemistry of Materials*, 2018, **30**, 2829-2837.
37. I. Goto, M. Itakura, S. Shibata, K. Honda, Y. Ide, M. Sadakane and T. Sano, *Microporous and Mesoporous Materials*, 2012, **158**, 117-122.
38. K. Honda, M. Itakura, Y. Matsuura, A. Onda, Y. Ide, M. Sadakane and T. Sano, *Journal of Nanoscience and Nanotechnology*, 2013, **13**, 3020-3026.
39. D. Schwalbe-Koda, Z. Jensen, E. Olivetti and R. Gómez-Bombarelli, *Nature Materials*, 2019, **18**, 1177-1181.
40. R. M. Barrer, *Zeolites*, 1981, **1**, 130-140.
41. D. Barthomeuf, G. Coudurier and J. C. Védrine, *Materials Chemistry and Physics*, 1988, **18**, 553-575.
42. P. P. E. A. de Moor, T. P. M. Beelen, B. U. Komanschek, L. W. Beck, P. Wagner, M. E. Davis and R. A. van Santen, *Chemistry—A European Journal*, 1999, **5**, 2083-2088.
43. C. S. Cundy and P. A. Cox, *Chemical Reviews*, 2003, **103**, 663-702.
44. C. S. Cundy and P. A. Cox, *Microporous and Mesoporous Materials*, 2005, **82**, 1-78.
45. M. E. Davis, *Chemistry of Materials*, 2014, **26**, 239-245.

46. K. Itabashi, Y. Kamimura, K. Iyoki, A. Shimojima and T. Okubo, *Journal of the American Chemical Society*, 2012, **134**, 11542-11549.
47. S. Alfaro, C. Rodriguez, M. A. Valenzuela and P. Bosch, *Materials Letters*, 2007, **61**, 4655-4658.
48. F. J. Machado, C. M. López, M. a. A. Centeno and C. Urbina, *Applied Catalysis A: General*, 1999, **181**, 29-38.
49. R. A. Rakoczy, M. Breuninger, M. Hunger, Y. Traa and J. Weitkamp, *Chemical Engineering & Technology*, 2002, **25**, 273-275.
50. H. Lee, S. I. Zones and M. E. Davis, *Nature*, 2003, **425**, 385-388.
51. H. Zhang, Q. Guo, L. Ren, C. Yang, L. Zhu, X. Meng, C. Li and F.-S. Xiao, *Journal of Materials Chemistry*, 2011, **21**, 9494-9497.
52. T. Yokoi, M. Yoshioka, H. Imai and T. Tatsumi, *Angewandte Chemie International Edition*, 2009, **48**, 9884-9887.
53. Y. Wang, X. Wang, Q. Wu, X. Meng, Y. Jin, X. Zhou and F.-S. Xiao, *Catalysis Today*, 2014, **226**, 103-108.
54. Y. Kamimura, K. Iyoki, S. P. Elangovan, K. Itabashi, A. Shimojima and T. Okubo, *Microporous and Mesoporous Materials*, 2012, **163**, 282-290.
55. Y. Suzuki, T. Wakihara, K. Itabashi, M. Ogura and T. Okubo, *Topics in Catalysis*, 2009, **52**, 67-74.
56. L. Van Tendeloo, E. Gobechiya, E. Breyneart, J. A. Martens and C. E. A. Kirschhock, *Chemical Communications*, 2013, **49**, 11737-11739.
57. C. Baerlocher, L. B. McCusker and D. H. Olson, *Atlas of Zeolite Framework Types*, Elsevier, Amsterdam, 6 edn., 2007.
58. M. J. Frisch, G. W. Trucks, H. B. Schlegel, G. E. Scuseria, M. A. Robb, J. R. Cheeseman, G. Scalmani, V. Barone, B. Mennucci, G. A. Petersson, H. Nakatsuji, M. Caricato, X. Li, H. P. Hratchian, A. F. Izmaylov, J. Bloino, G. Zheng, J. L. Sonnenberg, M. Hada, M. Ehara, K. Toyota, R. Fukuda, J. Hasegawa, M. Ishida, T. Nakajima, Y. Honda, O. Kitao, H. Nakai, T. Vreven, J. A. M. Jr., J. E. Peralta, F. Ogliaro, M. Bearpark, J. J. Heyd, E. Brothers, K. N. Kudin, V. N. Staroverov, R. Kobayashi, J. Normand, K. Raghavachari, A. Rendell, J. C. Burant, S. S. Iyengar, J. Tomasi, M. Cossi, N. Rega, J. M. Millam, M. Klene, J. E. Knox, J. B. Cross, V. Bakken, C. Adamo, J. Jaramillo, R. Gomperts, R. E. Stratmann, O. Yazyev, A. J. Austin, R. Cammi, C. Pomelli, J. W. Ochterski, R. L. Martin, K. Morokuma, V. G. Zakrzewski, G. A. Voth, P. Salvador, J. J. Dannenberg, S. Dapprich, A. D. Daniels, O. Farkas, J. B. Foresman, J. V. Ortiz, J. Cioslowski and D. J. Fox, 2014, Gaussian 09 (Revision D.01), Gaussian Inc., Wallingford, CT.
59. Y. Wang, P. Verma, X. Jin, D. G. Truhlar and X. He, *Proceedings of the National Academy of Sciences*, 2018, **115**, 10257-10262.
60. V. Barone and M. Cossi, *The Journal of Physical Chemistry A*, 1998, **102**, 1995-2001.
61. J. W. Ochterski, *Gaussian Inc*, 2000.
62. C. Baerlocher and L. B. McCusker, Database of Zeolite Structures: <http://www.iza-structure.org/databases/> (accessed August 2021).
63. S. A. Pelster, W. Schrader and F. Schüth, *Journal of the American Chemical Society*, 2006, **128**, 4310-4317.
64. E. J. J. Groenen, A. G. T. G. Kortbeek, M. Mackay and O. Sudmeijer, *Zeolites*, 1986, **6**, 403-411.
65. W. Loewenstein, *American Mineralogist: Journal of Earth and Planetary Materials*, 1954, **39**, 92-96.
66. R. F. Mortlock, A. T. Bell and C. J. Radke, *The Journal of Physical Chemistry*, 1991, **95**, 372-378.
67. R. F. Mortlock, A. T. Bell and C. J. Radke, *The Journal of Physical Chemistry*, 1991, **95**, 7847-7851.
68. R. K. Harris, J. Parkinson, A. Samadi-Maybodi and W. Smith, *Chemical Communications*, 1996, 593-594.
69. M. R. North and T. W. Swaddle, *Inorganic Chemistry*, 2000, **39**, 2661-2665.

70. K. Muraoka, W. Chaikittisilp and T. Okubo, *Journal of the American Chemical Society*, 2016, **138**, 6184-6193.
71. S. Mintova, N. H. Olson, V. Valtchev and T. Bein, *Science*, 1999, **283**, 958-960.
72. V. P. Valtchev, L. Tosheva and K. N. Bozhilov, *Langmuir*, 2005, **21**, 10724-10729.
73. V. P. Valtchev and K. N. Bozhilov, *The Journal of Physical Chemistry B*, 2004, **108**, 15587-15598.
74. X. Zhang, D. Q. Tong, J. J. Zhao and X. Y. Li, *Materials Letters*, 2013, **104**, 80-83.
75. H. J. Köroğlu, A. Sarioğlu, M. Tatlier, A. Erdem-Şenatalar and Ö. T. Savaşçı, *Journal of Crystal Growth*, 2002, **241**, 481-488.
76. E.-P. Ng, D. Chateigner, T. Bein, V. Valtchev and S. Mintova, *Science*, 2012, **335**, 70-73.
77. J. M. Chezeau, L. Delmotte, J. L. Guth and Z. Gabelica, *Zeolites*, 1991, **11**, 598-606.
78. H. L. Chen, J. Ding and Y. M. Wang, *New Journal of Chemistry*, 2014, **38**, 308-316.
79. Y. Shen, T. T. Le, R. Li and J. D. Rimer, *ChemPhysChem*, 2018, **19**, 529-537.
80. V. Vattipalli, A. M. Paracha, W. Hu, H. Chen and W. Fan, *Angewandte Chemie International Edition*, 2018, **57**, 3607-3611.
81. M. A. Cambor, A. Corma, P. Lightfoot, L. A. Villaescusa and P. A. Wright, *Angewandte Chemie International Edition*, 1997, **36**, 2659-2661.
82. P. A. Barrett, M. A. Cambor, A. Corma, R. H. Jones and L. A. Villaescusa, *Chemistry of Materials*, 1997, **9**, 1713-1715.
83. J. L. Jordá, F. Rey, G. Sastre, S. Valencia, M. Palomino, A. Corma, A. Segura, D. Errandonea, R. Lacomba and F. J. Manjón, *Angewandte Chemie*, 2013, **125**, 10652-10656.
84. S. Sang, F. Chang, Z. Liu, C. He, Y. He and L. Xu, *Catalysis Today*, 2004, **93**, 729-734.
85. G. Calleja, J. Pau and J. A. Calles, *Journal of Chemical & Engineering Data*, 1998, **43**, 994-1003.
86. P. Xie, Z. Ma, H. Zhou, C. Huang, Y. Yue, W. Shen, H. Xu, W. Hua and Z. Gao, *Microporous and Mesoporous Materials*, 2014, **191**, 112-117.
87. S. Gopal, K. Yoo and P. G. Smirniotis, *Microporous and Mesoporous Materials*, 2001, **49**, 149-156.
88. F. Geobaldo, S. Fiorilli, B. Onida, G. Giordano, A. Katovic and E. Garrone, *The Journal of Physical Chemistry B*, 2003, **107**, 1258-1262.
89. Z. Chen, S. Liu, H. Wang, Q. Ning, H. Zhang, Y. Yun, J. Ren and Y.-W. Li, *Journal of Catalysis*, 2018, **361**, 177-185.
90. S. I. Zones, *Chevron Research Co., US Patent 5,053,373*, 1991.
91. A. Molino, K. A. Łukaszuk, D. Rojo-Gama, K. P. Lillerud, U. Olsbye, S. Bordiga, S. Svelle and P. Beato, *Chemical Communications*, 2017, **53**, 6816-6819.
92. M. Zhang, H. Long, D. Fan, L. Wang, Q. Wang, Y. Chen, L. Sun and C. Qi, *Catalysis Science & Technology*, 2022, DOI: 10.1039/D1032CY00267A.
93. J. P. Foster and F. Weinhold, *Journal of the American Chemical Society*, 1980, **102**, 7211-7218.
94. J. J. Wolfis, D. E. P. Vanpoucke, A. Sharma, K. V. Lawler and P. M. Forster, *Microporous and Mesoporous Materials*, 2019, **277**, 184-196.
95. P. Demontis, G. B. Suffritti, S. Bordiga and R. Buzzoni, *Journal of the Chemical Society, Faraday Transactions*, 1995, **91**, 525-533.
96. A. Di Lella, N. Desbiens, A. Boutin, I. Demachy, P. Ungerer, J.-P. Bellat and A. H. Fuchs, *Physical Chemistry Chemical Physics*, 2006, **8**, 5396-5406.
97. M. A. Granato, T. J. Vlugt and A. E. Rodrigues, *Industrial & Engineering Chemistry Research*, 2007, **46**, 7239-7245.
98. M. J. Purdue and Z. Qiao, *Microporous and Mesoporous Materials*, 2018, **261**, 181-197.
99. R. M. Barrer and E. A. D. White, *Journal of the Chemical Society (Resumed)*, 1952, 1561-1571.
100. R. M. Barrer and J. W. Baynham, *Journal of the Chemical Society (Resumed)*, 1956, 2882-2891.

101. M. Iwama, Y. Suzuki, J. Plévert, K. Itabashi, M. Ogura and T. Okubo, *Crystal Growth & Design*, 2010, **10**, 3471-3479.
102. S. Ghojavand, E. B. Clatworthy, A. Vicente, E. Dib, V. Ruaux, M. Debost, J. El Fallah and S. Mintova, *Journal of Colloid and Interface Science*, 2021, **604**, 350-357.
103. M. Maldonado, M. D. Oleksiak, S. Chinta and J. D. Rimer, *Journal of the American Chemical Society*, 2013, **135**, 2641-2652.
104. A. Chawla, A. J. Mallette, R. Jain, N. Le, F. C. Robles-Hernandez and J. D. Rimer, *Microporous and Mesoporous Materials*, 2022, In Press.
105. S. Khodabandeh and M. E. Davis, *Microporous Materials*, 1997, **9**, 161-172.
106. J. V. Smith, F. Rinaldi and L. S. Dent Glasser, *Acta Crystallographica*, 1963, **16**, 45-53.
107. R. E. Morris, S. J. Weigel, N. J. Henson, L. M. Bull, M. T. Janicke, B. F. Chmelka and A. K. Cheetham, *Journal of the American Chemical Society*, 1994, **116**, 11849-11855.
108. Y. Liang, A. J. Jacobson and J. D. Rimer, *ACS Materials Letters*, 2020, **3**, 187-192.
109. D. Luo, Q. Wang, D. Fan, M. Yang, B. Fan, K. Cao, S. Xu, P. Tian and Z. Liu, *Microporous and Mesoporous Materials*, 2022, **329**, 111557.
110. M. G. Evans and M. Polanyi, *Transactions of the Faraday Society*, 1936, **32**, 1333-1360.
111. W. Li, M. G. Taylor, D. Bayerl, S. Mozaffari, M. Dixit, S. Ivanov, S. Seifert, B. Lee, N. Shanaiah and Y. Lu, *Nanoscale*, 2021, **13**, 206-217.
112. C. Liu, W. Gu, D. Kong and H. Guo, *Microporous and Mesoporous Materials*, 2014, **183**, 30-36.
113. N. Ren, J. Bronić, B. Subotić, Y.-M. Song, X.-C. Lv and Y. Tang, *Microporous and Mesoporous Materials*, 2012, **147**, 229-241.
114. R. E. Morris and J. Čejka, *Nature Chemistry*, 2015, **7**, 381-388.
115. A. J. Mallette, S. Seo and J. D. Rimer, *Nature Synthesis*, 2022, 1-14.